



Preparation of cobalt substituted zinc ferrite nanopowders via auto-combustion route: an investigation to their structural and magnetic properties

Jindi Feng¹ · Rui Xiong² · Yong Liu² · Fangyi Su¹ · Xueke Zhang¹

Received: 30 April 2018 / Accepted: 27 August 2018 / Published online: 31 August 2018
© Springer Science+Business Media, LLC, part of Springer Nature 2018

Abstract

$\text{Co}_x\text{Zn}_{1-x}\text{Fe}_2\text{O}_4$ ($x=0, 0.1, 0.2, 0.3, 0.4$) nanopowders were fabricated via auto-combustion synthesis followed by calcined treatment. The structural, morphological, compositional and magnetic properties of the as-synthesized samples were decided by X-ray diffraction (XRD), field emission scanning electron microscopy, energy dispersive X-ray spectroscopy, Fourier transform infrared spectroscopy, specific surface area and Physical Property Measurement System analyses, respectively. The XRD patterns revealed all annealed cobalt substituted zinc nanoferrites display a single phase cubic spinel structure, the decrease in lattice constant with increasing Co^{2+} ions concentration is related to the lattice shrinkage originated from the replacement of Zn^{2+} ions (ionic radii of 0.82 Å) by Co^{2+} ions (ionic radii of 0.78 Å); the increase of crystallite size with increasing Co^{2+} ions content can be attributed to the less exothermic for the formation of cobalt ferrite than that for zinc ferrite. The $M-H$ curves revealed that there are unsaturated magnetization and negligible hysteresis loops for all samples with lower cobalt concentration ($x=0, 0.1, 0.2,$ and 0.3), implying a superparamagnetic behavior; while the $\text{Co}_{0.4}\text{Zn}_{0.6}\text{Fe}_2\text{O}_4$ nanoparticles ($x=0.4$) show ferromagnetism at room temperature. The $M-T$ relations inferred the substitution of cobalt ions can remarkably enhance Curie temperature of the as-prepared Co–Zn ferrite nanoparticles. At room temperature lower cobalt-substituted zinc nanoferrites tend to show superparamagnetism while higher cobalt-substituted zinc nanoferrites prefer to present ferromagnetism.

1 Introduction

Spinel ferrites are generally recognized as a class of significant magnetic materials due to their versatile and promising medical, industrial and technological applications in catalysis, hyperthermia treatment, magnetic recording, MRI imaging, magnetic refrigeration, radio frequency circuits, sensors, high quality digital printing etc [1–4]. The molecular expression of a typical spinel ferrite bulk material can be denoted as MeFe_2O_4 , in which Me represents some divalent metal such as Co, Ni, Mn, Zn, Mg, Cu. Among various

spinel ferrites, zinc ferrite (ZnFe_2O_4) is a noted soft magnetic oxide due to the nonmagnetic characteristics of Zn^{2+} ions (the magnetic moment of Zn^{2+} is $0 \mu_B$), and it has been extensively developed and employed in electronics industry owing to its high magnetic permeability, large electric resistivity, low dielectric loss as well as low coercivity [5]. Compared to zinc ferrite, cobalt ferrite (CoFe_2O_4) is a remarkable hard magnetic material due to large magnetic moments of Co^{2+} ions (the magnetic moment of Co^{2+} is $3 \mu_B$), cobalt ferrite has played an important role in many practical fields especially related to magnetic storage, magnetic recording, actuators and catalysis on account of its prominent physical and chemical properties such as high coercivity, large magneto-crystalline anisotropy and fine chemical stability [6, 7]. As is known, zinc ions and cobalt ions both have very strong occupancy preference in spinel ferrite lattice, in which Zn^{2+} ions preferentially occupy the tetrahedral A sites while Co^{2+} ions tend to situate at the octahedral B sites [5, 8], consequently resulting in a normal spinel structure for zinc ferrite and an inverse spinel structure for cobalt ferrite.

✉ Jindi Feng
jdfeng84@hotmail.com

¹ School of Science and Technology, Xinyang College, No. 237, Nanhu Road, Shihe District, Xinyang City 464000, He'nan Province, People's Republic of China

² School of Physics and Key Laboratory of Acoustic and Photonic Materials and Devices of Ministry of Education, Wuhan University, Wuhan 430072, People's Republic of China

Single-phase structured ZnFe_2O_4 is evidently magnetically and structurally different from single-phase structured CoFe_2O_4 , in a sense they are even opposite with each other. The mixed-phase structured Co–Zn ferrite systems can be easily obtained by the introduction of cobalt ions dopant, in which the substitution of nonmagnetic Zn^{2+} ions with magnetic Co^{2+} ions alters the cation distribution of the previous zinc ferrite spinel lattice, leading to notable changes in the super-exchange interaction between the tetrahedral A sites and octahedral B sites, subsequently yielding noticeable modifications in magnetic parameters such as saturation magnetization M_s , coercivity H_c and Curie temperature T_c . It has long been verified that compared to their bulk counterpart, nanocrystalline Co–Zn ferrite materials usually own more complicated spinel structure which can be written as $(\text{Me}_{1-i}^{2+}\text{Fe}_i^{3+})^A[\text{Me}_i^{2+}\text{Fe}_{2-i}^{3+}]^B\text{O}_4$, in which the term i , namely degree of inversion, represents the percentage of tetrahedral A sites situated by Fe^{3+} ions while Me^{2+} denotes the divalent metal ions (Zn^{2+} , Co^{2+}) occupying tetrahedral sites or octahedral sites [9]. Degree of inversion i , influencing greatly on the distribution of Zn^{2+} , Co^{2+} and Fe^{3+} cations in nanostructured Co–Zn spinel ferrite lattice, is related closely to the preparation techniques [5, 8].

During the past decades, in many fields of science and technology, in order to control particle growth, increase specific surface area, tune particle shape and reduce energy losses existed in bulk powders, researchers have developed different techniques to prepare various functional inorganic metallic nanostructures, like ultrasonic irradiation method, self-assembly approach, electrospinning, spray pyrolysis, one-step solvothermal synthesis, oxidative polymerization process, citrate reduction wet chemical method [10–17]. Generally in nanoscale cobalt–zinc ferrite systems different synthesis techniques and procedures generate different cation distribution, thus magnetic parameters and ferromagnetic–paramagnetic (FM–PM) transition temperature (namely Curie temperature T_c) may be strikingly altered. Jnaneshwara et al. synthesized $\text{Co}_{1-x}\text{Zn}_x\text{Fe}_2\text{O}_4$ ($0 \leq x \leq 0.5$) nanoferrites employing low temperature solution combustion method and found the crystallite sizes were in the range of 12–18 nm, they uncovered that with increasing zinc ions doping content, magnetic properties such as saturation magnetization M_s , coercivity H_c and anisotropy constant k decreased continuously [18]. Singh et al. reported the fabrication of a series of nano-crystalline particles with an average crystallite size of 6–8 nm and sphere shape of visible light responsive Zn–Co ferrites with formula $\text{Zn}_{1-x}\text{Co}_x\text{Fe}_2\text{O}_4$ ($x=0, 0.2, 0.4, 0.6, 0.8$ and 1.0) via reverse micelle technique using sodium dodecyl sulfate as the surfactant agent, they came to a conclusion that the as-prepared nanoparticles presented a transition from ferromagnetism to superparamagnetism (FM–SPM) with increasing zinc concentration [8]. Sharifi and Shokrollahi systematically investigated the

structure and magnetism of $\text{Co}_{1-x}\text{Zn}_x\text{Fe}_2\text{O}_4$ ($0.5 < x < 0.75$) nanoparticles synthesized by chemical co-precipitation route. They revealed that for Co–Zn ferrites the grain growth was hindered by the existence of zinc dopant while the lattice parameter increased continuously with increasing the zinc substitution content, the saturation magnetization, coercivity and Curie temperature weakened steadily by increasing the zinc content, the sample $\text{Co}_{0.3}\text{Zn}_{0.7}\text{Fe}_2\text{O}_4$ ($x=0.7$) demonstrated SPM and its Curie point was 97°C [19]. Phan et al. fabricated a series of $\text{Zn}_{1-x}\text{Co}_x\text{Fe}_2\text{O}_4$ nanoparticles by utilizing hydrothermal method, they reported that the average crystallite sizes were in the scope of 16–22 nm and the phase transition temperature T_c (FM–PM) increased from 606 K for ZnFe_2O_4 ($x=0$) to 823 K for CoFe_2O_4 ($x=1$) [5].

Although plenty of research work on structural and magnetic properties of zinc–cobalt ferrite nanomaterials has been reported, until now, to the best of our knowledge, there are few investigations dealing with the structure and magnetism of $\text{Co}_x\text{Zn}_{1-x}\text{Fe}_2\text{O}_4$ nanoferrite systems by employing auto-combustion route. Auto-combustion route possesses several advantages such as relatively good physical homogeneity, low degree of agglomeration and narrow distribution of particle size in synthesizing highly purified and crystallized nanocomposites [20]. Meanwhile auto-combustion method characterizes itself with low reaction temperature, cheap reactant, simple processing, high yield as well as large specific surface area due to plenty of gases released during ignition [7]. In the present work, we fabricated a series of $\text{Co}_x\text{Zn}_{1-x}\text{Fe}_2\text{O}_4$ ($x=0, 0.1, 0.2, 0.3, 0.4$) nanoparticles by auto-combustion synthesis using citric acid as the fuel, then we studied the effect of Co substitution on the structural and magnetic properties of the as-fabricated $\text{Co}_x\text{Zn}_{1-x}\text{Fe}_2\text{O}_4$ nanoparticles. There are mainly the following three reasons for this study: (i) till now there are few literature reported about the structural and magnetic properties of cobalt–zinc nanoferrites synthesized by auto-combustion route, this research aims to gain more insight into this issue; (ii) it's reported that Co–Zn mixed structured ferrite nanomaterials have shown great potential in some applications like self-controlled hyperthermia due to their high sensitivity of magnetization to temperature [21, 22]. In the auto-combustion synthesis process the reaction temperature can be easily manipulated, makes it possible to meet the requirements for hyperthermia apparatuses and therapies. (iii) at present Co–Zn ferrite systems have been gradually applied to catalyze some hazardous organics such as aniline and phenol [23, 24], therefore it's technologically significant to synthesize Co–Zn nanoferrites with large surface area. Obviously the auto-combustion synthesis adopted in this work is suitable to yield Co–Zn nanoferrites with large surface area, due to a large amount of gases released during combustion will produce plenty of pores in the Co–Zn ferrite nanoparticles.

2 Experimental

2.1 Synthesis process

$\text{Co}_x\text{Zn}_{1-x}\text{Fe}_2\text{O}_4$ ($x=0, 0.1, 0.2, 0.3, 0.4$) nanoparticles were synthesized by auto-combustion synthesis. The starting reagents used were all of analytical grade and purchased from Sinopharm Chemical Reagent Co., Ltd., Shanghai, P.R. China, and they were all employed without further purification. All the reagents were used stoichiometrically as shown in Table 1. The desired samples were obtained by the following procedure:

Under fierce stirring, 100 mL citric acid (with concentration 0.3 mol/L) solution (acted as a solvent and stabilizer) were added into 50 mL metal nitrates solution consisting of stoichiometric $\text{Zn}(\text{NO}_3)_2 \cdot 6\text{H}_2\text{O}$ (with concentration $0.2(1-x)$ mol/L), $\text{Co}(\text{NO}_3)_2 \cdot 6\text{H}_2\text{O}$ (with concentration $0.2x$ mol/L) and $\text{Fe}(\text{NO}_3)_3 \cdot 9\text{H}_2\text{O}$ (with concentration 0.4 mol/L). The ratio of the fuel (citric acid) to the oxidizer (metal nitrates) is defined as ϕ . According to the redox reaction theory, the ratio of fuel to oxidizer is not the molar quantity ratio of citric acid to metal nitrates, it signifies generally ratio of the total oxidation valence to the total reduction valence of all the reagents (do not include O_2 resulted from air) [7, 25]. In light of Table 1 and the overall redox reaction Eq. (1f) given in Sect. 3.1, there are following relations:

$$\frac{\text{Molar quantity of citric acid}}{\text{Molar quantity of cobalt nitrate and zinc nitrate}} = \frac{20\phi/9}{x+1-x} = \frac{0.03 \text{ mol}}{0.01 \text{ mol}},$$

we obtain the ratio of the fuel to the oxidizer $\phi = 1.35$.

The mixed solution was maintained at 60 °C under fierce stirring for 15 min. After this the uniformly blended complex solution was heated up on a stirring hot plate. When the complex solution arrived at its boiling point, the evaporation of water took place and the evaporation process persisted until the solution evaporated to dryness. At this moment, due to the exothermic reaction, the remnant in the plate ignited

sharply for just a few seconds, later it immediately turned into ashes (namely dry precursors). Thereafter, all the as-synthesized dried precursors were divided into two portions, one portion was ground directly into powders (namely dried precursors) while the other portion was annealed at 800 °C for 5 h in air so as to gain desired Co–Zn ferrite nanoparticles with chemically stable and highly crystallized structure, eventually, it was also ground into fine powders (namely annealed samples).

2.2 Measurements

The phase structure and X-ray density of all the as-synthesized samples were determined by using X-ray diffraction (XRD) (D8 Advanced X-ray Diffractometer) at room temperature with Cu K α radiation ($\lambda = 1.5406 \text{ \AA}$, operated at 40 kV and 35 mA) in the 2θ range from 25° to 65°. Before recording the XRD patterns, a small amount of standard Si powders were added into the samples to eliminate the errors originated from position calibration of the X-ray beam. The instrumental broadening, computed by utilizing the (111) peak of Si sample was found to be 0.69 Å. Field emission scanning electron microscope [field-emission scanning electron microscope (FE-SEM), Sirion 200, equipped with energy dispersive X-ray spectroscopy (EDS)] was employed to analyse the morphology, nanostructure and elemental composition of the samples. All the investigated samples were coated with carbon before SEM and EDS analysis. Fourier transform infrared spectroscopy (FT-IR) analysis was carried out on Nicolet FTIR 5700 from 4000 to 400 cm^{-1} . The specific surface area measurements were implemented on an Accelerated Surface Area and Porosimetry System (Micromeritics ASAP-2020) after degasification of all as-synthesized samples in vacuum at 200 °C for 3 h in order to eliminate the adsorbates. The magnetic properties were decided by employing a Physical Property Measurement System (PPSM-9, Quantum Design). The hysteresis loops of all the annealed samples were measured at room temperature in an applied magnetic field from –15,000 to 15,000 Oe. Zero-field cooled (ZFC) and field cooled (FC) measurements were conducted at an applied magnetic field of 200 Oe with the temperature changing from 10 to 375 K, the phase transition

Table 1 The amount of all the reagents for the preparation of $\text{Co}_x\text{Zn}_{1-x}\text{Fe}_2\text{O}_4$ ($x=0, 0.1, 0.2, 0.3, 0.4$) nanoparticles given in grams ($\phi = 1.35$)

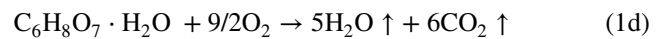
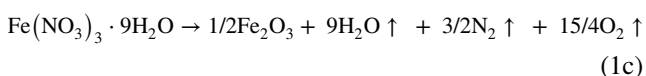
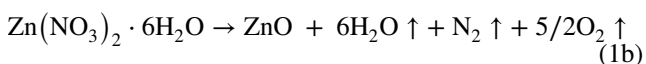
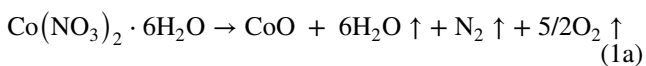
Reagents	x=0	x=0.1	x=0.2	x=0.3	x=0.4
$\text{Co}(\text{NO}_3)_2 \cdot 6\text{H}_2\text{O}$	0 mol	0.001 mol	0.002 mol	0.003 mol	0.004 mol
	0 g	0.2910 g	0.5821 g	0.8731 g	1.1641 g
$\text{Zn}(\text{NO}_3)_2 \cdot 6\text{H}_2\text{O}$	0.01 mol	0.009 mol	0.008 mol	0.007 mol	0.006 mol
	2.9749 g	2.6774 g	2.3799 g	2.0824 g	1.7849 g
$\text{Fe}(\text{NO}_3)_3 \cdot 9\text{H}_2\text{O}$	0.02 mol	0.02 mol	0.02 mol	0.02 mol	0.02 mol
	8.08 g	8.08 g	8.08 g	8.08 g	8.08 g
$\text{C}_6\text{H}_8\text{O}_7 \cdot \text{H}_2\text{O}$	0.03 mol	0.03 mol	0.03 mol	0.03 mol	0.03 mol
	6.3042 g	6.3042 g	6.3042 g	6.3042 g	6.3042 g

temperatures of FM to PM were also determined from the measurements.

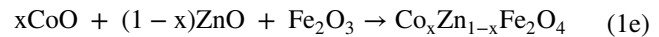
3 Results and discussion

3.1 XRD analysis

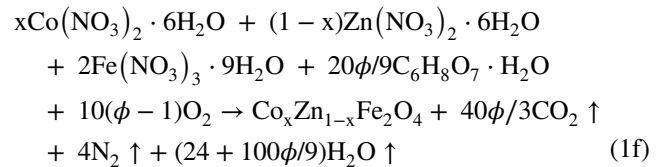
Generally, in the auto-combustion synthesis, heating, evaporation of the solvent, formation and decomposition of the gel, self-ignition, combustion, annealing and formation of the desired nanoferrite powders proceed in one technological step. The driving force for the auto-combustion synthesis is the tendency of the system to reduce its Gibbs free energy G by converting the chemical potential into heat. When the temperature of the solutions is increased to the reaction onset point, an exothermic chemical reaction initiates, accompanied with the further temperature increase of reaction solutions, which in turn results into acceleration of the reaction rate, therefore the reaction process is self-accelerating. The process ends only if the reagents had been completely converted into products and arrived at an equilibrium state in which the Gibbs energy G is minimum [25]. In this research, during the process of auto-combustion route, the solutions of the metal nitrate salts and citric acid, acting as oxidizer and fuel respectively, are sufficiently exothermic to retain a self-sustained chemical reaction. The ratio of fuel to oxidizer is usually named as ϕ . ϕ represents a variable where $\phi = 1$ represents that the initial reagents do not need atmospheric oxygen to complete the auto-combustion reaction, while $\phi > 1$ (or $\phi < 1$) means fuel rich (or fuel lean) conditions [7, 25]. According to the redox reaction theory, the ratio of fuel to oxidizer ϕ refers generally to the total oxidation valence and the total reduction valence of the reagents (do not include O_2 resulted from air), and the ratio of these two are used as the stoichiometric ratio coefficient of the fuel and oxidizer [7, 25]. It is necessary to be noted that the function of the fuel is not only to offer enough heat for the whole reaction process, but also to increase the solubility of the metal nitrates, to prevent selective precipitation of the metal ions during water evaporation and thus to guarantee the formation of stable desired Co–Zn ferrite nanoparticles [26]. It is assumed that CO_2 , H_2O and N_2 are all gaseous products formed in the combustion reaction. Thus in this research, the balance of the metal nitrates reduction reaction (Eqs. 1a–1c) and fuel (citric acid) oxidation reaction (Eq. 1d) can be expressed as follows [25]:



During the stage of the self-sustained combustion the metal oxide CoO, ZnO and Fe_2O_3 reacts further with each other and leads to the desired Co–Zn mixed structured nanopowders, as shown in Eq. (1e).



Equations (1a–1e) are demonstrated as the growth mechanism for the formation of $Co_xZn_{1-x}Fe_2O_4$ nanoferrite systems based on the redox chemistry theory [25]. The overall redox reaction is displayed as follows:



It's obvious to see in Eq. (1f) that the amount of gaseous products increases steadily with the increase of fuel to oxidizer ratio ϕ . A large amount of gaseous products released from the combustion reaction causes much more porosity and inhibition of agglomeration in the as-burnt powders, leading to a large specific surface area. However, the excess amount of gaseous products leads to the lower combustion temperature and less crystalline products [7, 25]. According to research results of Pourgolmohammad et al. for ratio of fuel to oxidizer $\phi \geq 1$, due to the large amount of gaseous products, the higher purity of the cobalt ferrite nanoparticles leads to the maximum saturation magnetization [7]. Thus in this work, we choose $\phi = 1.35$ in order to obtain good magnetic properties.

To study the phase composition, lattice parameter, average crystallite size, X-ray density as well as the porosity, the XRD patterns of all the 800 °C annealed $Co_xZn_{1-x}Fe_2O_4$ ($x=0, 0.1, 0.2, 0.3, 0.4$) nanopowders were recorded at room temperature in detail and the results are demonstrated in Fig. 1. As is well known, the cobalt–zinc mixed structured spinel ferrite is identified by the reflection peaks indexed to (220), (311), (222), (400), (422), (511), and (440) reflection planes characteristic of the faced-centered cubic (FCC) spinel structure [19, 27]. The close study with the Miller indexed diffraction peaks indicate all the measured samples are highly crystallized and single phased in a FCC spinel structure, being classified to the space group $Fd\bar{3}m$, and without any obvious secondary phase. All XRD peaks are in accordance with the JCPDS card no. 22-1086 (for cubic spinel $CoFe_2O_4$) and 89-1012 (for cubic spinel $ZnFe_2O_4$). Figure 1 reveals that when the cobalt substitution content x changes from 0 to 0.4, diffraction peaks for the same crystal planes (hkl) shift slightly to higher 2θ diffraction angles; this is mostly resulted from the smaller ionic radius of doping Co^{2+} (0.78 Å) compared to that of Zn^{2+} (0.82 Å). Therefore,

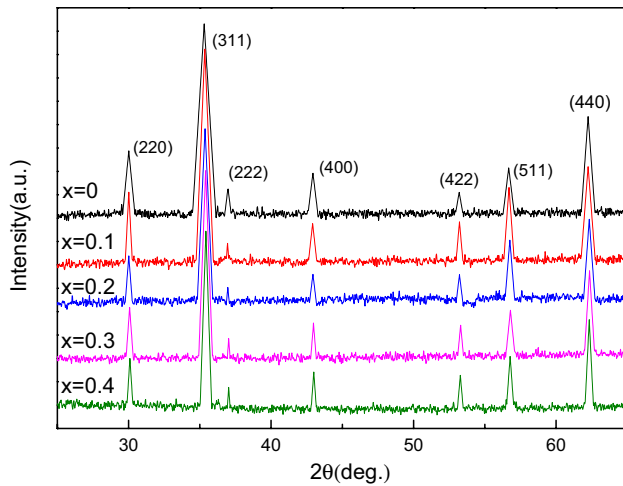


Fig. 1 XRD patterns of the as-prepared $\text{Co}_x\text{Zn}_{1-x}\text{Fe}_2\text{O}_4$ nanopowders with various Co substitution content

following the increase of Co^{2+} content in the Co–Zn spinel ferrite lattice, the volume of the spinel phase unit cell shrinks and consequently leads to the decrease in the distance between crystal planes. In order to evaluate in detail the effect of cobalt substitution on the crystal structure of zinc ferrites, the lattice constant was calculated by utilizing the magnitudes of Miller indices and d -spacing from the well-known equation,

$$a = \frac{\lambda \sqrt{h^2 + k^2 + l^2}}{2 \sin \theta_{hkl}} \quad (2)$$

where (hkl) is the Miller indices, θ_{hkl} represents the diffraction peak corresponding to the (hkl) crystal plane, and λ denotes the X-ray wavelength of Cu $K\alpha$ and it takes 1.5406 Å. The calculation results of the lattice constant values for all the as-prepared Co–Zn nanoferrites are presented in Table 2. It is evident from Table 2 that the lattice constant a decreases steadily with increasing Co ions substitution concentration x , and it is in good agreement with Vegard's law, just as displayed in Table 2 and Fig. 2 [28, 29]. With the cobalt substitution content x increasing from 0 to 0.4, the lattice constant decreases almost linearly from 8.423 Å (for ZnFe_2O_4) to 8.398 Å (for $\text{Co}_{0.4}\text{Zn}_{0.6}\text{Fe}_2\text{O}_4$).

Table 2 Lattice constant (a), crystallite size (D), X-ray density (ρ_x), bulk density (ρ) and porosity (P) of the as-prepared $\text{Co}_x\text{Zn}_{1-x}\text{Fe}_2\text{O}_4$ nanopowders

Comp.	Lattice constant a (Å)	Crystallite size D (nm)	X-ray density ρ_x (g/cm^3)	Bulk density ρ (g/cm^3)	Porosity (%) P
$x=0$	8.423	14.1	5.367	5.172	3.63
$x=0.1$	8.415	17.6	5.342	5.161	3.39
$x=0.2$	8.409	19.2	5.324	5.153	3.21
$x=0.3$	8.401	23.2	5.305	5.149	2.94
$x=0.4$	8.398	25.4	5.277	5.136	2.68

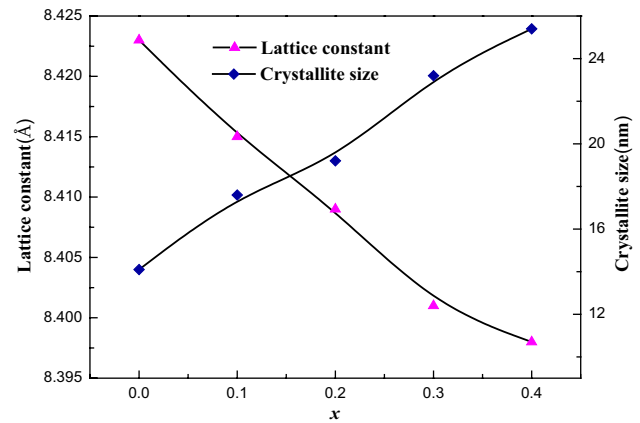


Fig. 2 The variations in lattice constant (a) and average crystallite size (D) of the as-prepared $\text{Co}_x\text{Zn}_{1-x}\text{Fe}_2\text{O}_4$ nanopowders with Co concentration x

This phenomenon can be interpreted as follows: As Zn^{2+} ions show strong tetrahedral A sites preference while Co^{2+} ions tend to situate at octahedral B sites, meanwhile Fe^{3+} ions can reside at both A sites and B sites, thus with the gradual replacement of Co^{2+} ions by Zn^{2+} ions, on the one hand a portion of Fe^{3+} ions migrate from B sites to A sites and cause the continuous substitution of Zn^{2+} ions with Fe^{3+} ions at A sites; on the other hand a portion of Fe^{3+} ions at B sites are substituted with the doping Co^{2+} ions, consequently the lattice shrinks, due to the smaller ionic radii of Co^{2+} doping ions (0.78 Å) and Fe^{3+} ions (0.67 Å) compared to those of Zn^{2+} ions (0.82 Å) [27, 30].

As illustrated in Sect. 2.2, all the as-prepared samples were mixed with a little amount of standard Si powders to minimize errors resulted from the position calibration of X-ray beam, and the instrumental broadening, computed by utilizing the (111) peak of Si sample was found to be 0.69. To evaluate the effect of cobalt substitution on the crystallite size of all as-synthesized $\text{Co}_x\text{Zn}_{1-x}\text{Fe}_2\text{O}_4$ ($x=0, 0.1, 0.2, 0.3, 0.4$) nanopowders, we calculated the average crystallite size D according to the most intense (311) peaks of the XRD spectra by employing the famous Debye–Scherrer relation and considering the line-broadening analysis,

$$D = \frac{0.89\lambda}{\beta \cos \theta_{311}} \quad (3)$$

where λ is the wavelength of Cu $K\alpha$, β denotes the full width of the strongest (311) peak at half maximum in radians (2θ) (the instrumental broadening has been eliminated), θ_{311} represents the position at the most intense diffraction peak (311). Table 2 displays the calculated values of the average crystallite sizes with the variation of Co substitution concentration. The evolution relation of crystallite size D as a function of cobalt content x is drawn in Fig. 2 and obviously it demonstrates a near linear relationship between D and x . When Co ions doping content x varies from 0 to 0.4, the average crystallite size increases monotonously from 14.1 nm (for ZnFe_2O_4) to 25.4 nm (for $\text{Co}_{0.4}\text{Zn}_{0.6}\text{Fe}_2\text{O}_4$). Evidently the addition of Co ions into the nano-sized zinc ferrites is in favor of the grain growth of the crystal. The following factors can be responsible for this fact:

- (1) Due to the strong tetrahedral site preference of Zn^{2+} ions, zinc ferrite is a typical normal spinel ferrite and it is more exothermic compared to the inverse spinel structured cobalt ferrite. It is reported that ZnFe_2O_4 has a formation enthalpy of -2.7 kcal/mol. Therefore, with the Zn^{2+} ions being gradually replaced with Co^{2+} ions, less heat will be released, it will lead to increasing of the molecular concentration at the surface of the crystal and thus promote the grain growth [19].
- (2) As is well known, Co^{2+} ions behave more dynamically with oxygen anions and ligands as compared to that for Zn^{2+} ions, due to the incomplete electronic configuration of Co^{2+} ions ($3d^7$), in contrast Zn^{2+} ions ($3d^{10}$) have complete electronic configuration. Thus with the gradual introduction of the Co^{2+} ions into the zinc ferrite, the covalent interaction would be reinforced and subsequently the grain growth yields continuously.

Values of the X-ray density ρ_X of all the as-synthesized Co–Zn ferrite samples were computed by utilizing the following equation [9, 27],

$$\rho_X = \frac{8M}{N_A a^3} \quad (4)$$

where M is molecular weight for the nanoferrite, N_A represents the Avogadro's constant and a denotes the corresponding lattice constant. Table 2 shows the calculated values of the X-ray density ρ_X for each composition in light of the relation (4). It's found from Table 2 that the magnitude of X-ray density ρ_X decreases with increasing of cobalt substitution content x . As is known X-ray density is proportional to the molecular weight while it is inversely proportional to the cubic of lattice constant. With the gradual introduction of Co doping ions, lattice constant decreases and the molecular weight of the $\text{Co}_x\text{Zn}_{1-x}\text{Fe}_2\text{O}_4$ decreases as well, due to the smaller molecular weight value for the

CoFe_2O_4 ($M_{\text{CoFe}_2\text{O}_4} = 234.6$ g/mol) than that for the ZnFe_2O_4 ($M_{\text{ZnFe}_2\text{O}_4} = 241.1$ g/mol). The X-ray density is expected to keep lowering down with the increase of cobalt concentration x , this can be ascribed to the quicker weakening speed of the molecular weight M with ρ_X than that of the a^3 with ρ_X . The bulk density ρ can be measured by using the liquid immersion method, the measurement results for all samples are displayed in Table 2. It's easy to find that the bulk density ρ (experimental density) is very close to its corresponding X-ray density ρ_X (theoretical density) for all samples and both of them show a similar decreasing trend with increasing cobalt content, as is presented in Fig. 3. The differences between the two densities can be attributed to the pores existent in the samples. To evaluate the effect of pores to the crystal structure, porosity P is defined as follows,

$$P = (1 - \rho / \rho_X) \times 100\% \quad (5)$$

the porosity values were computed in light of the Eq. (5) and the results are listed in Table 2. It is revealed that the porosity is lowering with the increase of cobalt substitution concentration, just as is shown in Fig. 3. This can be ascribed to the increase of grain size, with the Zn^{2+} ions being gradually replaced by Co^{2+} ions, the grain growth is promoted and thus it leads to fewer pores in the cobalt–zinc spinel ferrite lattice. The phenomenon about the porosity being obstructed by grain growth is in accordance with that reported by Anwar et al. [27] and Hashim et al. [31].

3.2 EDS and SEM analysis

Figure 4 shows the surface morphology and chemical composition of $\text{Co}_x\text{Zn}_{1-x}\text{Fe}_2\text{O}_4$ ($x = 0, 0.2, 0.4$) nanoparticles measured by FE-SEM equipped with EDS. Concentrations of the elements in the weight (wt%) and atomic (at.%) percentage present in $\text{Co}_x\text{Zn}_{1-x}\text{Fe}_2\text{O}_4$ ($x = 0, 0.2, 0.4$)

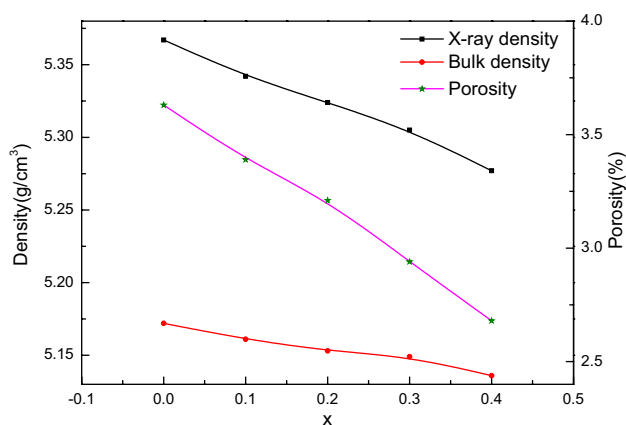


Fig. 3 The variation in X-ray density (ρ_X), bulk density (ρ) and porosity (P) of the as-prepared $\text{Co}_x\text{Zn}_{1-x}\text{Fe}_2\text{O}_4$ nanopowders with Co substitution concentration x

nanoparticles obtained from EDS analysis has been presented in Table 3. It is obvious that the presence of Zn, Co, Fe and O has been confirmed from the EDS spectra. The

data listed in Table 3 indicate that the atomic and weight percentages of elements are nearly consistent with the expected theoretical composition ratio. The signal of C in all the EDS

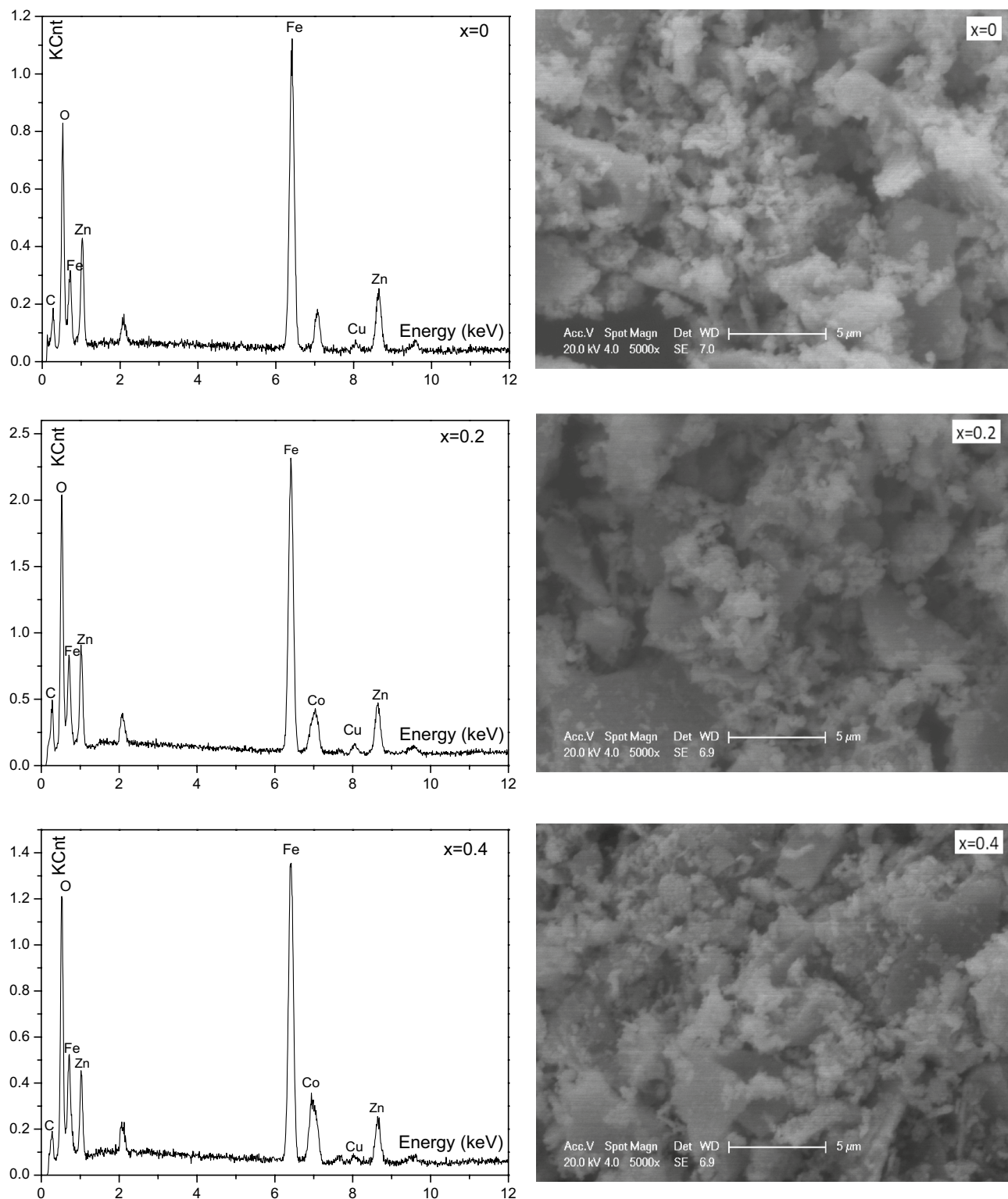
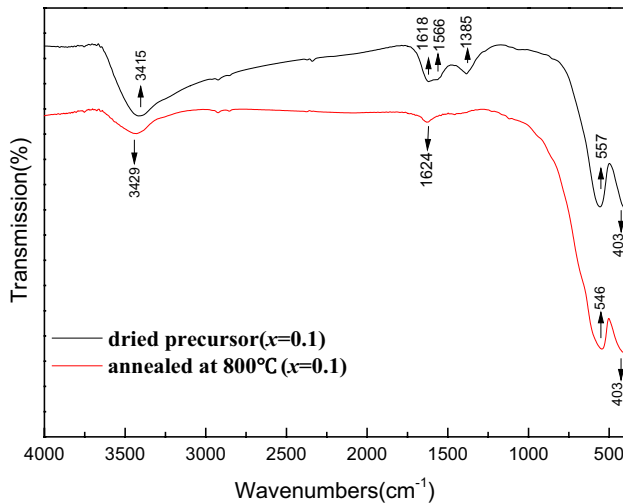


Fig. 4 EDS spectra and SEM images of the typical $\text{Co}_x\text{Zn}_{1-x}\text{Fe}_2\text{O}_4$ nanopowders for Co content $x=0, 0.2, 0.4$, respectively

Table 3 Concentrations of the elements in the weight (wt%) and atomic (at.%) percentage present in $\text{Co}_x\text{Zn}_{1-x}\text{Fe}_2\text{O}_4$ ($x=0, 0.2, 0.4$) nanoparticles obtained from EDS analysis

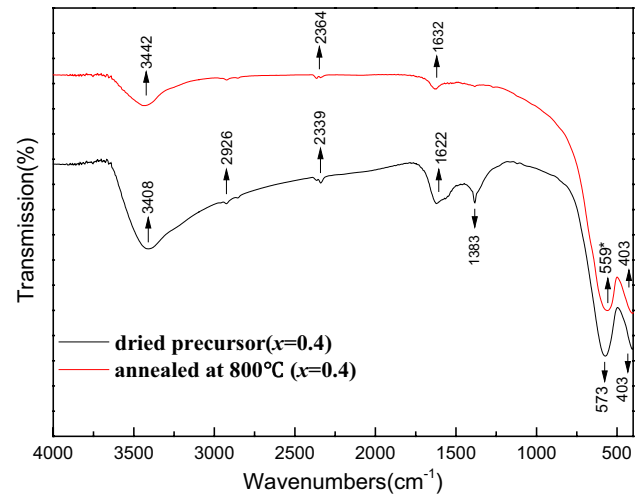
x	Zn		Co		Fe		O	
	wt%	at.%	wt%	at.%	wt%	at.%	wt%	at.%
0	27.71	17.19	0	0	52.12	37.86	16.91	42.86
0.2	22.20	13.24	5.64	3.73	50.02	34.92	18.94	46.15
0.4	17.39	10.40	11.56	07.67	50.48	35.34	18.55	45.34

**Fig. 5** FT-IR spectra of $\text{Co}_{0.1}\text{Zn}_{0.9}\text{Fe}_2\text{O}_4$ as-burnt dried precursor and 800 °C-annealed nanopowders, respectively

spectra is due to treatment of being coated with carbon prior to SEM and EDS measurement, meanwhile a very small peak of Cu appeared in all investigated EDS spectra which might be attributed to the copper grid. The SEM images of the cobalt substituted zinc ferrites with $x=0, 0.2, 0.4$ are also listed in Fig. 4 and they show the particles are homogeneous and uniformly distributed for all investigated samples. They also show that smaller particles in the micrographs have the sizes < 100 nm, meanwhile all samples indicate the existence of soft agglomeration.

3.3 FT-IR spectroscopy

Figure 5 shows the IR spectra of the $\text{Co}_{0.1}\text{Zn}_{0.9}\text{Fe}_2\text{O}_4$ ($x=0.1$) dried precursors and its counterpart annealed at 800 °C spontaneously, while the IR spectra of the $\text{Co}_{0.4}\text{Zn}_{0.6}\text{Fe}_2\text{O}_4$ ($x=0.4$) dried precursors and $\text{Co}_{0.4}\text{Zn}_{0.6}\text{Fe}_2\text{O}_4$ ($x=0.4$) calcined nanopowders are presented in Fig. 6. The broad absorption band situated at 3415 cm^{-1} and 3408 cm^{-1} respectively in the dried gel are related to the stretching modes of the absorbed water, for the annealed samples these absorption bands shift to 3429 cm^{-1} and 3442 cm^{-1} respectively [19]. The peaks at 1618 cm^{-1} and 1622 cm^{-1} for the dried precursors are originated from the stretching vibrations of carboxylate (COO^-), in IR spectra of the annealed samples

**Fig. 6** FT-IR spectra of $\text{Co}_{0.4}\text{Zn}_{0.6}\text{Fe}_2\text{O}_4$ as-burnt dried precursor and 800 °C-annealed nanopowders, respectively

these peaks are inconspicuous, indicating the elimination of the remnant organics by high temperature heat treatment [7]. The appearance of the peaks at 1385 cm^{-1} and 1383 cm^{-1} for the dried precursors are resulted from anti-symmetric NO_3^- bond, its complete absence in the IR spectra of annealed samples reveals that the residual NO_3^- impurities had been thoroughly removed by the annealing process [7, 32]. It's well known that there exists two primary metal–oxygen absorption bands ν_1 and ν_2 in the IR spectra for nanomaterials with spinel ferrite structure. The higher frequency band ν_1 relates to the stretching modes of metal ions at the tetrahedral sites, $\text{M}_{\text{tetra}} \leftrightarrow \text{O}$, while the lower frequency band ν_2 corresponds to the stretching modes of metal ions at the octahedral sites, $\text{M}_{\text{octa}} \leftrightarrow \text{O}$ [14, 33–35]. In the present work, according to Figs. 5 and 6, the characteristic band at the lower wavenumbers ν_2 keeps unchanged, irrelevant to the cobalt substitution concentration or the annealing procedure; while for the higher frequency absorption band ν_1 , things are quite different. The characteristic absorption band peak ν_1 for $\text{Co}_{0.1}\text{Zn}_{0.9}\text{Fe}_2\text{O}_4$ annealed nanoparticles is centered at 546 cm^{-1} , while for $\text{Co}_{0.4}\text{Zn}_{0.6}\text{Fe}_2\text{O}_4$ annealed nanoparticles the $\text{M}_{\text{tetra}} \leftrightarrow \text{O}$ bands ν_1 shifts slightly to 559 cm^{-1} (highlighted with an asterisk in Fig. 6). The shift of the $\text{M}_{\text{tetra}} \leftrightarrow \text{O}$ characteristic bands ν_1 to higher wavenumbers with increasing cobalt substitution content can be attributed to the lighter atomic mass of the substitution cobalt than that of zinc [28].

3.4 Analysis of specific surface area

The analyses of the specific surface area for all calcined cobalt–zinc ferrite nanoparticles with various cobalt doping concentration were recorded by employing Nitrogen adsorption static volumetric technique. After all the as-prepared $\text{Co}_x\text{Zn}_{1-x}\text{Fe}_2\text{O}_4$ ferrite nanoparticles being degassed in vacuum at 200 °C for 3 h in order to eliminate the adsorbates adherent to the samples, the measurement of the specific surface area per unit mass S_w , was conducted and thus we computed the equivalent particle size d of all the as-prepared $\text{Co}_x\text{Zn}_{1-x}\text{Fe}_2\text{O}_4$ nanopowders according to the following relation [36],

$$d = 6/(\rho \times S_w) \quad (6)$$

in which ρ denotes density of the sample and it can be taken as 5.30 g/cm^3 . The experimental data of the specific surface area S_w and its related estimated equivalent particle sizes for different cobalt-substituted zinc ferrite nanopowders are shown in Table 4. It is found the as-synthesized nanosized powders have large specific surface area. This is because a large amount of released gases such as CO_2 , N_2 and vapor of water produced during the combustion reaction tend to obstruct the formation of a compact composition and disperse the large particles to produce nanoparticles. In light of Eq. (6), small particle size means large specific surface area, it's obvious from Table 4 that the specific surface area S_w reduces steadily with the enhancement of the cobalt substitution concentration, the values of S_w decrease monotonously from $121.6 \text{ m}^2/\text{g}$ for ZnFe_2O_4 ($x=0$) to $41.0 \text{ m}^2/\text{g}$ for $\text{Co}_{0.4}\text{Zn}_{0.6}\text{Fe}_2\text{O}_4$ ($x=0.4$) with x ranging from 0 to 0.4. Correspondingly, the equivalent particle size d increases gradually from 9.3 nm for ZnFe_2O_4 ($x=0$) to 27.6 nm for $\text{Co}_{0.4}\text{Zn}_{0.6}\text{Fe}_2\text{O}_4$ ($x=0.4$) with x varying from 0 to 0.4, due to inversely proportional relationship between d and S_w , as is shown in Eq. (6). Table 4 shows the comparison of the equivalent particle size d decided by specific surface area test and the average crystallite size D evaluated by XRD analysis for each composition, evidently they are consistent well with each other. By means of analyses above mentioned, the introduction of cobalt ions dopant facilitates the

Table 4 Specific surface area (S_w), equivalent particle size (d) and crystallite size (D) of the as-prepared $\text{Co}_x\text{Zn}_{1-x}\text{Fe}_2\text{O}_4$ nanopowders

Comp.	Specific surface area S_w (m^2/g)	Equivalent particle size d (nm)	Crystallite size D (nm)
$x=0$	121.6	9.3	14.1
$x=0.1$	95.8	11.8	17.6
$x=0.2$	68.1	16.6	19.2
$x=0.3$	48.8	23.2	23.2
$x=0.4$	41.0	27.6	25.4

grain growth of $\text{Co}_x\text{Zn}_{1-x}\text{Fe}_2\text{O}_4$ nanopowders. The following reason may be responsible for this: electronegativity of Co^{2+} ions is larger than that of Zn^{2+} ions, and this makes Co^{2+} ions more advantageous to pass through the grain boundaries and arrive at the neighbouring vacancies and subsequently leads to the growth of the particles [19].

3.5 Magnetic properties

Figure 7 displays the variations of magnetization as a function of the applied magnetic fields at room temperature for the annealed samples with different cobalt substitution concentration. The applied magnetic field adopted in the measurements is ranging from -15 to 15 kOe . Significant magnetic properties, including maximum magnetization M_m , remnant magnetization M_r , coercivity field H_C of all nanoferrites with different Co content are presented in Table 5. It's observed in Fig. 7 that for all as-prepared $\text{Co}_x\text{Zn}_{1-x}\text{Fe}_2\text{O}_4$ nanopowders except $x=0.4$ the saturation magnetization could not be reached even on condition that the applied magnetic field had been enhanced up to 15 kOe . For samples with cobalt doping content $x=0, 0.1, 0.2$ and 0.3 , the corresponding maximum magnetization values M_m are 1.91 emu/g , 4.15 emu/g , 10.37 emu/g and 23.80 emu/g , respectively; while for $\text{Co}_{0.4}\text{Zn}_{0.6}\text{Fe}_2\text{O}_4$ nanopowders ($x=0.4$) the saturation magnetization M_S (i.e. for sample with $x=0.4$ M_S is equal to M_m) can be arrived at and its value is 41.46 emu/g .

It's found the $M-H$ curves of all samples measured at room temperature show a typical 'S'-like shape. The hysteresis loops of the samples with Co content $x=0, 0.1, 0.2$ and 0.3 display no eminent hysteresis, no saturation magnetization and negligible coercivity and remnant magnetization, indicating the SPM for ZnFe_2O_4 , $\text{Co}_{0.1}\text{Zn}_{0.9}\text{Fe}_2\text{O}_4$, $\text{Co}_{0.2}\text{Zn}_{0.8}\text{Fe}_2\text{O}_4$ and $\text{Co}_{0.3}\text{Zn}_{0.7}\text{Fe}_2\text{O}_4$ nanopowders at room temperature [19, 37, 38]. Comparatively the $M-H$ curve of the sample with $x=0.4$ reveals a small hysteresis with the values of saturation magnetization, remnant magnetization and coercivity being 41.46 emu/g , 2.635 emu/g and 22.62 Oe , respectively, demonstrating the ferromagnetism (FM) for $\text{Co}_{0.4}\text{Zn}_{0.6}\text{Fe}_2\text{O}_4$ nanoparticles [39, 40]. It's implied the significant phase transition from superparamagnetic to ferromagnetic state (SPM \rightarrow FM) will be produced by the introduction of Co^{2+} ions into ZnFe_2O_4 nanopowders. The low cobalt doping concentration x in stimulating the superparamagnetic behavior for Co–Zn mixed-structured ferrite nanoparticles can be explained as follows: (1) As Co^{2+} ions are magnetic ions with magnetic moment of $3 \mu_B$ while Zn^{2+} ions are non-magnetic ions, thus in $\text{Co}_x\text{Zn}_{1-x}\text{Fe}_2\text{O}_4$ nanoferrites with low cobalt content the super-exchange coupling between tetrahedral A sites and octahedral B sites is much more weakened, resulting in a superparamagnetic behavior. (2) It was reported that SPM was usually observed in

Fig. 7 The M – H loops (at room temperature) of the as-prepared $\text{Co}_x\text{Zn}_{1-x}\text{Fe}_2\text{O}_4$ nanopowders (included inset of the high magnified M – H curves)

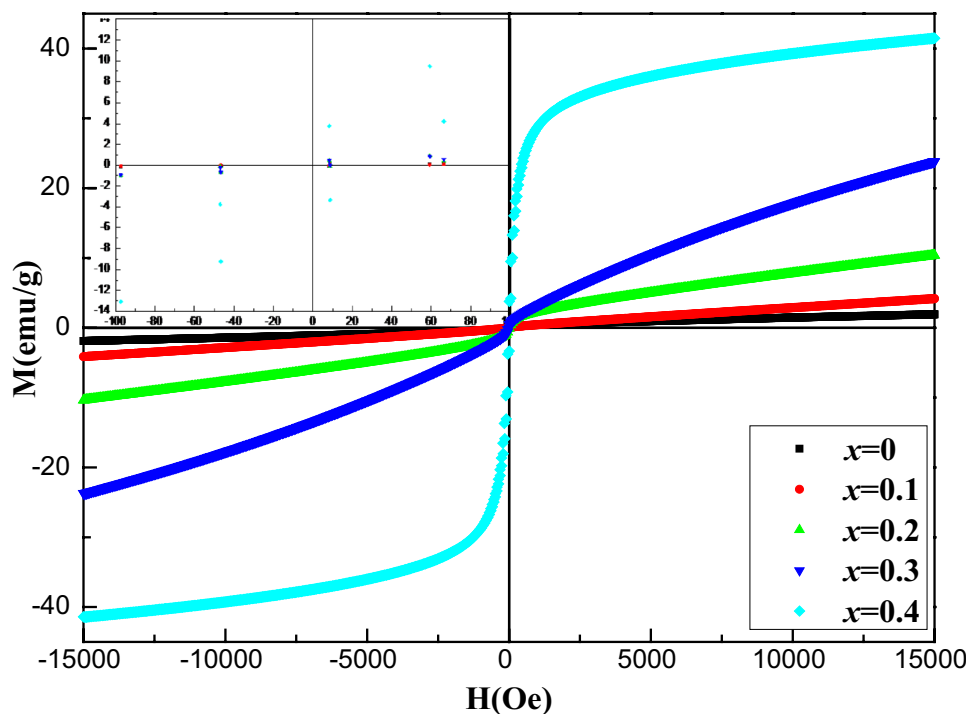


Table 5 Maximum magnetization (M_m), remnant magnetization (M_r), coercivity (H_C) and Curie temperature (T_C) of the as-prepared $\text{Co}_x\text{Zn}_{1-x}\text{Fe}_2\text{O}_4$ nanopowders

Comp.	M_m (emu/g)	M_r (emu/g)	H_C (Oe)	T_C (K)
$x=0$	1.91	0.026	1.57	38
$x=0.1$	4.15	0.034	3.34	82
$x=0.2$	10.37	0.054	8.18	97
$x=0.3$	23.80	0.082	17.51	171
$x=0.4$	41.46	2.635	22.62	341

samples with grain sizes in the scope of 10–24 nm regarded as critical size for the superparamagnetic domains [9, 41]. While bigger particles tend to show ferromagnetism, smaller particles tend to behave as superparamagnetic. In the present work, according to Table 4 we have known the particle sizes of all samples except $\text{Co}_{0.4}\text{Zn}_{0.6}\text{Fe}_2\text{O}_4$ ($x=0.4$) belong to the scope of the superparamagnetic critical size. Therefore the exhibition of SPM at room temperature for ZnFe_2O_4 , $\text{Co}_{0.1}\text{Zn}_{0.9}\text{Fe}_2\text{O}_4$, $\text{Co}_{0.2}\text{Zn}_{0.8}\text{Fe}_2\text{O}_4$ and $\text{Co}_{0.3}\text{Zn}_{0.7}\text{Fe}_2\text{O}_4$ nanoparticles is reasonable.

Generally the variation of the magnetic parameters such as M_s and H_C with different cobalt substitution content in Table 5 can be ascribed to the cation stoichiometry and cation distribution among the tetrahedral A sites and octahedral B sites. Figure 8 presents the developing trend of M_m (for $x=0.4$ it equals to M_s) and H_C as a function of cobalt doping content. According to Neel's two sublattices model, saturation magnetization is primarily decided by the

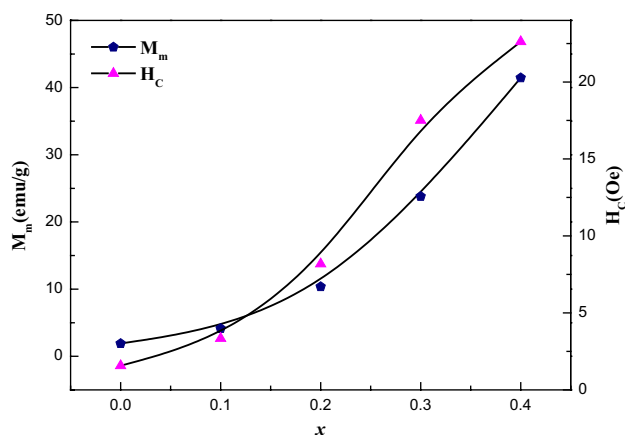


Fig. 8 The maximum magnetization (M_m) and coercivity (H_C) (at room temperature) in an applied field up to $\pm 15,000$ Oe as a function of Co substitution content x for the as-prepared $\text{Co}_x\text{Zn}_{1-x}\text{Fe}_2\text{O}_4$ nanopowders

super-exchange interaction between A and B sites [28]. With the replacement of non-magnetic zinc ions (with magnetic moment of $0 \mu_B$ and strong A sites preference) by magnetic cobalt ions (with magnetic moment of $3 \mu_B$ and strong B sites preference), the super-exchange coupling between the two sublattices strengthens and it eventually leads to the increase of the saturation magnetization. As is well known, coercivity H_C is usually determined by the magneto-crystalline anisotropy, in the nanoscale cobalt–zinc ferrite systems the single-ion anisotropy of Co^{2+} ions located at B sites could be responsible for the magnitude of magneto-crystalline

anisotropy [5, 18]. Following the increasing of cobalt substitution content, the higher concentration of Co^{2+} ions at the octahedral sites should cause a continuous increase in the magneto-crystalline anisotropy and thus bring about a steady increase in the coercivity H_C .

In order to investigate the effect of cobalt substitution content on magnetic transition temperature (namely Curie temperature T_C) from the FM \rightarrow PM, the magnetization as a function of temperature ranging from 10 to 375 K in an applied field of 200 Oe was measured. The M - T curves displayed in Fig. 9 reveal that all as-synthesized $\text{Co}_x\text{Zn}_{1-x}\text{Fe}_2\text{O}_4$ nanoferrites show a transition from ferromagnetic behavior to paramagnetic behavior with the increase of temperature. The Curie temperature T_C is determined as the temperature at which the dM/dT versus T reaches the minimum [27]. It reveals from Table 5 that the T_C values of the samples with cobalt doping content $x=0, 0.1, 0.2, 0.3, 0.4$ are 38 K, 82 K, 97 K, 171 K and 341 K, respectively. The curve of T_C values as a function of x was graphed in Fig. 10 and it shows that the Curie temperature increases steadily with increasing Co^{2+} ions substitution concentration. This can be explained by the reinforcement of the super-exchange interaction among A–B

intra-sublattice due to the replacement of non-magnetic Zn^{2+} ions with magnetic Co^{2+} ions. As Co^{2+} ions prefer to occupy the B sites while Zn^{2+} ions tend to situate at A sites, with the gradual substitution of Zn^{2+} ions (magnetic moment of $0 \mu_B$) with Co^{2+} ions (magnetic moment of $3 \mu_B$), the magnetic Fe^{3+} ions (magnetic moment of $5 \mu_B$) are forced to migrate from B sites to A sites and thus strengthen remarkably the magnetic moment at the A sites, leading to the increase in A–B intra-sublattice coupling and promotion of Curie temperature [29]. According to the results of Curie temperature T_C and calculated particle size d presented in Tables 4 and 5, it's reasonable to find that the as-combusted ZnFe_2O_4 , $\text{Co}_{0.1}\text{Zn}_{0.9}\text{Fe}_2\text{O}_4$, $\text{Co}_{0.2}\text{Zn}_{0.8}\text{Fe}_2\text{O}_4$ and $\text{Co}_{0.3}\text{Zn}_{0.7}\text{Fe}_2\text{O}_4$ nanopowders should all show a superparamagnetic behavior at room temperature, due to the lower Curie temperature of these nanoferrites than room temperature and their particle sizes all belonging to the scope of critical diameter for the superparamagnetic domains (10–24 nm); while sample $\text{Co}_{0.4}\text{Zn}_{0.6}\text{Fe}_2\text{O}_4$ should exhibit ferromagnetism at room temperature, for its Curie temperature (341 K) is higher than room temperature and its particle size is without the critical size for SPM as well. This deduction is in a good agreement

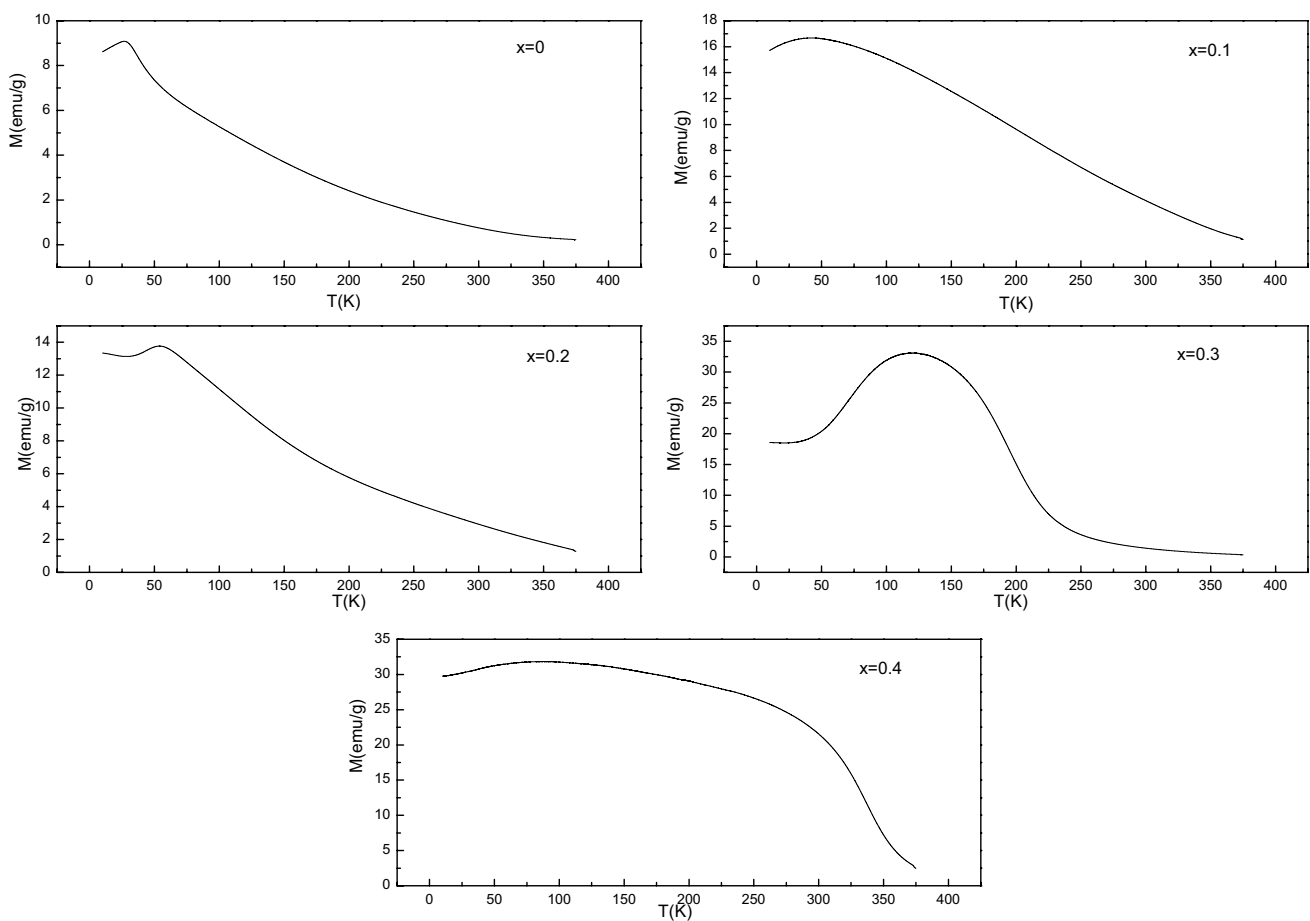


Fig. 9 The M - T relationship of the as-prepared $\text{Co}_x\text{Zn}_{1-x}\text{Fe}_2\text{O}_4$ nanopowders with various Co concentration x in the applied field of 200 Oe

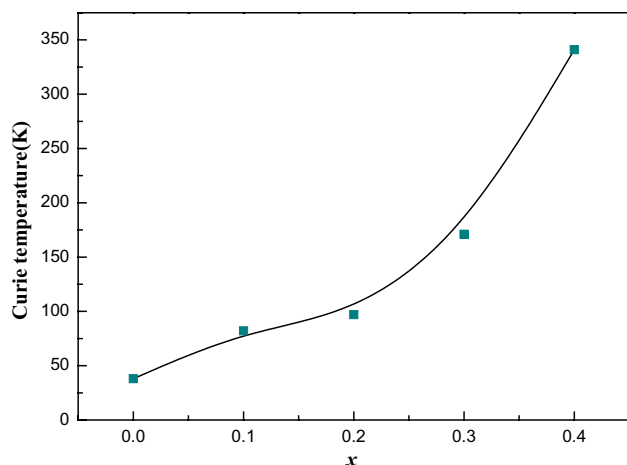


Fig. 10 The Curie temperature (T_c) as a function of Co doping content for the as-prepared $\text{Co}_x\text{Zn}_{1-x}\text{Fe}_2\text{O}_4$ nanopowders

with our investigation on the room temperature $M-H$ curves for all samples, where the room temperature hysteresis loops of ZnFe_2O_4 , $\text{Co}_{0.1}\text{Zn}_{0.9}\text{Fe}_2\text{O}_4$, $\text{Co}_{0.2}\text{Zn}_{0.8}\text{Fe}_2\text{O}_4$ and $\text{Co}_{0.3}\text{Zn}_{0.7}\text{Fe}_2\text{O}_4$ nanopowders all show SPM while sample $\text{Co}_{0.4}\text{Zn}_{0.6}\text{Fe}_2\text{O}_4$ exhibits ferromagnetism.

ZFC and FC $M-T$ curves for $\text{Co}_{0.2}\text{Zn}_{0.8}\text{Fe}_2\text{O}_4$, $\text{Co}_{0.3}\text{Zn}_{0.7}\text{Fe}_2\text{O}_4$ and $\text{Co}_{0.4}\text{Zn}_{0.6}\text{Fe}_2\text{O}_4$ nanoparticles with temperature ranging from 10 to 375 K were measured in an applied field of 200 Oe and they are presented in Fig. 11. In ZFC measurements, the samples were initially cooled from room temperature to 10 K without applying an external magnetic field. After arriving at 10 K, a magnetic field of 200 Oe was applied and then the magnetization was recorded as the temperature varied from 10 to 375 K. As is demonstrated in Fig. 11, with rising up of temperature, the magnetization of $\text{Co}_{0.2}\text{Zn}_{0.8}\text{Fe}_2\text{O}_4$ nanoparticle increases and approaches its maximum at the blocking temperature (55 K), T_B , thereafter the magnetization value weakens rapidly with further increasing of temperature. The FC curve of magnetization versus temperature for $\text{Co}_{0.2}\text{Zn}_{0.8}\text{Fe}_2\text{O}_4$ nanoferrites exhibit almost the same path as ZFC curve. According to the ZFC curve of $\text{Co}_{0.3}\text{Zn}_{0.7}\text{Fe}_2\text{O}_4$ revealed in Fig. 11, the magnetization firstly increases with increasing of temperature, and reaches the maximum at the blocking temperature (122 K), subsequently it reduces sharply. The divergence between the ZFC and the FC curves for $\text{Co}_{0.2}\text{Zn}_{0.8}\text{Fe}_2\text{O}_4$ and $\text{Co}_{0.3}\text{Zn}_{0.7}\text{Fe}_2\text{O}_4$ nanopowders implies there is a non-equilibrium magnetization below their reversibility temperatures, T_{irr} , representing the blocking

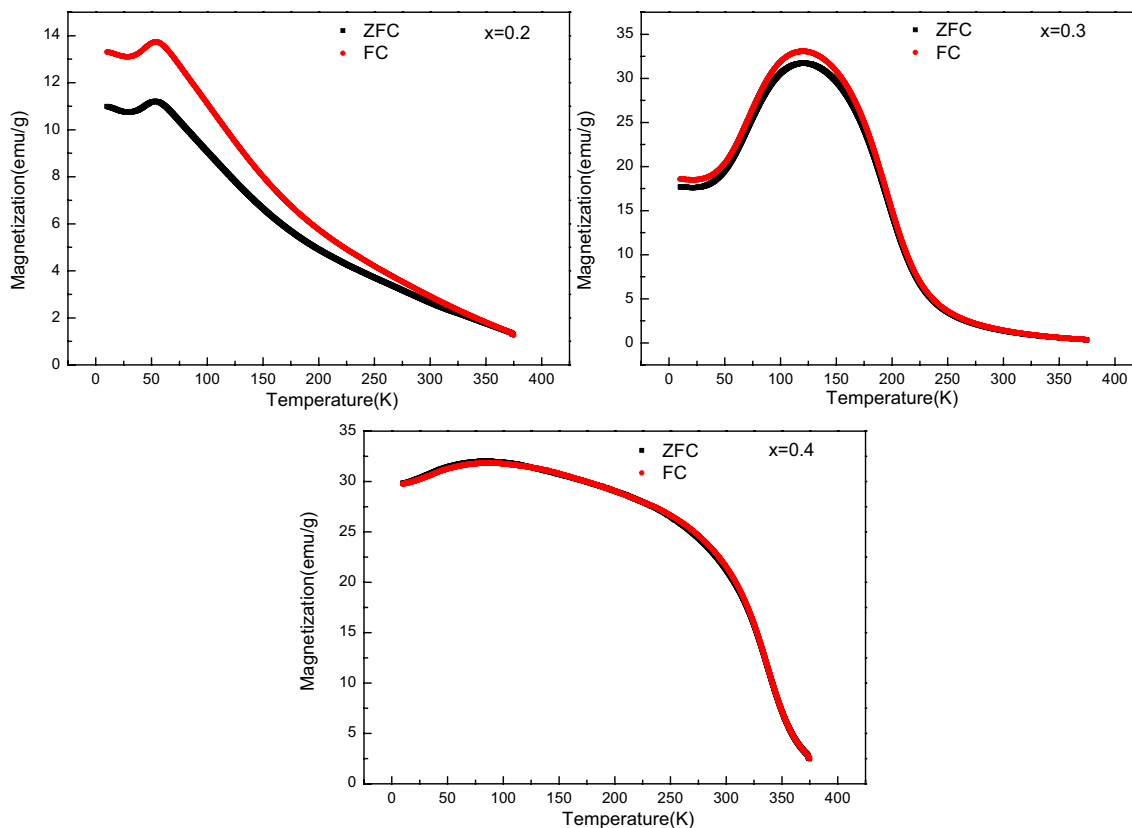


Fig. 11 The ZFC and FC curves of the as-prepared $\text{Co}_x\text{Zn}_{1-x}\text{Fe}_2\text{O}_4$ nanopowders ($x=0.2, 0.3, 0.4$) with various Co concentration in an applied field of 200 Oe

temperature of particles with the highest energy barrier for the ZFC case, the values of T_{irr} for $\text{Co}_{0.2}\text{Zn}_{0.8}\text{Fe}_2\text{O}_4$ and $\text{Co}_{0.3}\text{Zn}_{0.7}\text{Fe}_2\text{O}_4$ are 357 K and 246 K, respectively [28, 40]. As regards to these two samples, within the temperature between the blocking temperature and the Curie temperature, though the thermal energy is incapable of overcoming the coupling force between neighboring atoms, it is sufficient to change the direction of magnetization of the entire crystallite, leading to the disappearance of hysteresis behavior and thus an earlier exhibition of SPM below Curie temperature [37, 40]. In light of Fig. 11, the ZFC and FC curves of $\text{Co}_{0.4}\text{Zn}_{0.6}\text{Fe}_2\text{O}_4$ nanoparticles coincides wholly with each other, implying a ferromagnetic state below its Curie temperature (341 K).

4 Conclusions

The nano-structured cobalt substituted $\text{Co}_x\text{Zn}_{1-x}\text{Fe}_2\text{O}_4$ ($x=0, 0.1, 0.2, 0.3, 0.4$) ferrite systems were fabricated by employing auto-combustion route. The study of the XRD patterns showed single-phased cubic spinel structure for all as-synthesized calcined samples, the lattice constant decreases with increasing of cobalt substitution concentration due to the relatively smaller ionic radii of Co^{2+} ions (0.78 Å) than those of Zn^{2+} ions (0.82 Å), the increase in average crystallite size with increase of Co^{2+} ions content can be ascribed to the less exothermic for the formation of cobalt ferrite than that for zinc ferrite. The bulk density ρ and the X-ray density ρ_x for all samples exhibit a similar decreasing trend with increasing cobalt doping content, the differences between the two densities can be attributed to the pores existing in the samples. The EDS analysis confirmed the elements present in the as-synthesized samples and agreed well with theoretical values. The analyses of IR spectra indicated that the impurities involved in the dried precursors such as nitrates, carboxylate and absorbed water were successfully eliminated by 800 °C annealing treatment. The shift of the $M_{\text{tetra}} \leftrightarrow O$ characteristic bands ν_1 to higher wavenumbers with increasing cobalt content is attributed to the lighter atomic mass of the cobalt than that of zinc. The investigation of $M-H$ curves at room temperature showed a superparamagnetic behavior for all samples with lower cobalt doping concentration ($x=0, 0.1, 0.2,$ and 0.3) except for $x=0.4$, while the $\text{Co}_{0.4}\text{Zn}_{0.6}\text{Fe}_2\text{O}_4$ nanoparticles ($x=0.4$) show saturated magnetization and small hysteresis loop, indicating the ferromagnetism at room temperature, this is in accordance with the analyses of Curie temperature. It's found at room temperature the magnetic phase of the as-prepared cobalt-substituted zinc ferrite nanoparticles tend to transform from the superparamagnetic to the ferromagnetic by increasing the cobalt doping content.

Acknowledgements This work is supported by National Natural Science Foundation of China (No. 51571152), Research Fund for the Key Scientific Program of Higher Education of He'nan Province of China (No. 17B430006), Research fund of He'nan Provincial Training Program of Innovation and Entrepreneurship for Undergraduates (No. 201713503002), Research fund of Xinyang College Training Program of Innovation and Entrepreneurship for Undergraduates (No. CX20170003).

References

1. A.R. Shyam, R. Dwivedi, V.S. Reddy, K.V.R. Chary, R. Prasad, Vapour phase methylation of pyridine with methanol over the $\text{Zn}_{1-x}\text{Mn}_x\text{Fe}_2\text{O}_4$ ($x = 0, 0.25, 0.50, 0.75$ and 1) ferrite system. *Green Chem.* **4**, 558–561 (2002)
2. Y. Köseoğlu, H. Kavas, Size and surface effects on magnetic properties of Fe_3O_4 nanoparticles. *J. Nanosci. Nanotechnol.* **8**, 584–590 (2008)
3. S. Deka, P.A. Joy, Enhanced permeability and dielectric constant of NiZn ferrite synthesized in nanocrystalline form by a combustion method. *J. Am. Ceram. Soc.* **90**, 1494–1499 (2007)
4. K. Khan, A. Maqsood, M.A. Rehman, M.A. Malik, M. Akram, Structural, dielectric, and magnetic characterization of nanocrystalline Ni–Co ferrites. *J. Supercond. Nov. Magn.* **25**, 2707–2711 (2012)
5. T.L. Phan, N. Tran, D.H. Kim, N.T. Dang, D.H. Manh, T.N. Bach, C.L. Liu, B.W. Lee, Magnetic and magnetocaloric properties of $\text{Zn}_{1-x}\text{Co}_x\text{Fe}_2\text{O}_4$ nanoparticles. *J. Electron. Mater.* **46**, 4214–4226 (2017)
6. C.N. Chinnasamy, B. Jeyadevan, O.P. Perez, K. Shinoda, K. Tohji, A. Kasuya, Growth dominant co-precipitation process to achieve high coercivity at room temperature in CoFe_2O_4 nanoparticles. *IEEE Trans. Magn.* **38**, 2640–2642 (2002)
7. B. Pourgolmohammad, S.M. Masoudpanah, M.R. Aboutalebi, Synthesis of CoFe_2O_4 powders with high surface area by solution combustion method: effect of fuel content and cobalt precursor. *Ceram. Int.* **43**, 3797–3803 (2017)
8. C. Singh, S. Jauhar, V. Kumar, J. Singh, S. Singhal, Synthesis of zinc substituted cobalt ferrites via reverse micelle technique involving in situ template formation: a study on their structural, magnetic, optical and catalytic properties. *Mater. Chem. Phys.* **156**, 188–197 (2015)
9. M. Atif, M. Nadeem, Sol-gel synthesis of nanocrystalline $\text{Zn}_{1-x}\text{Ni}_x\text{Fe}_2\text{O}_4$ ceramics and its structural, magnetic and dielectric properties. *J. Sol-Gel. Sci. Technol.* **72**, 615–626 (2014)
10. Y.P. Zhang, S.H. Lee, K.R. Reddy, A.I. Gopalan, K.P. Lee, Synthesis and characterization of core-shell SiO_2 nanoparticles/poly (3-aminophenylboronic acid) composites. *J. Appl. Polym. Sci.* **104**, 2743–2750 (2007)
11. K.R. Reddy, K.P. Lee, A.I. Gopalan, Self-assembly directed synthesis of poly (ortho-toluidine)-metal (gold and palladium) composite nanospheres. *J. Nanosci. Nanotechnol.* **7**, 3117–3125 (2007)
12. S. Kim, M. Kim, Y.K. Kim, S.H. Hwang, S.K. Lim, Core-shell-structured carbon nanofiber-titanate nanotubes with enhanced photocatalytic activity. *Appl. Catal. B* **148–149**, 170–176 (2014)
13. K.R. Reddy, V.G. Gomes, M. Hassan, Carbon functionalized TiO_2 nanofibers for high efficiency photocatalysis. *Mater. Res. Express* **1**, 015012 (2014)
14. M.S. Arif Sher Shah, K. Zhang, A.R. Park, K.S. Kim, N.G. Park, J.H. Park, P.J. Yoo, Single-step solvothermal synthesis of mesoporous Ag- TiO_2 -reduced graphene oxide ternary composites with enhanced photocatalytic activity. *Nanoscale* **5**, 5093–5101 (2013)

15. T. Lu, R. Zhang, C. Hu, F. Chen, S. Duo, Q. Hu, TiO₂-graphene composites with exposed {001} facets produced by a one-pot solvothermal approach for high performance photocatalyst. *Phys. Chem. Chem. Phys.* **15**, 12963–12970 (2013)
16. K.R. Reddy, K.P. Lee, A.I. Gopalan, M.S. Kim, A. Md Showkat, Y.C. Nho, Synthesis of metal (Fe or Pd)/alloy (Fe–Pd)-nanoparticles-embedded multiwall carbon nanotube/sulfonated polyaniline composites by γ irradiation. *J. Polym. Sci. A* **44**, 3355–3364 (2006)
17. K.R. Reddy, K.P. Lee, A.I. Gopalan, Self-assembly approach for the synthesis of electro-magnetic functionalized Fe₃O₄/polyaniline nanocomposites: effect of dopant on the properties. *Colloid Surf. A* **320**, 49–56 (2008)
18. D.M. Jnaneshwara, D.N. Avadhani, B. Daruka Prasad, B.M. Nagabhushana, H. Nagabhushana, S.C. Sharma, S.C. Prashantha, C. Shivakumara, Effect of zinc substitution on the nanocobalt ferrite powders for nanoelectronic devices. *J. Alloys Compd.* **587**, 50–58 (2014)
19. I. Sharifi, H. Shokrollahi, Nanostructural, magnetic and Mössbauer studies of nanosized Co_{1-x}Zn_xFe₂O₄ synthesized by coprecipitation. *J. Magn. Magn. Mater.* **324**, 2397–2403 (2012)
20. K.H. Wu, Y.C. Chang, G.P. Wang, Preparation of NiZn ferrite/SiO₂ nanocomposite powders by sol–gel auto-combustion method. *J. Magn. Magn. Mater.* **269**(2), 150–155 (2004)
21. G. Vaidyanathan, S. Sendhilnathan, Characterization of Co_{1-x}Zn_xFe₂O₄ nanoparticles synthesized by co-precipitation method. *Physica B* **403**, 2157–2167 (2008)
22. I. Sharifi, H. Shokrollahi, S. Amiri, Ferrite-based magnetic nanofluids used in hyperthermia applications. *J. Magn. Magn. Mater.* **324**, 903–915 (2012)
23. K. Sreekumar et al., A comparison on the catalytic activity of Zn_{1-x}Co_xFe₂O₄ (x = 0, 0.2, 0.5, 0.8 and 1.0)-type ferrosinels prepared via. A low temperature route for the alkylation of aniline and phenol using methanol as the alkylating agent. *J. Appl. Catal. A* **230**(1–2), 245 (2002)
24. K. Sreekumar, T.M. Jyothi, T. Mathew et al., Selective N-methylation of aniline with dimethyl carbonate over Zn_{1-x}Co_xFe₂O₄ (x = 0, 0.2, 0.5, 0.8 and 1.0) type systems. *J. Mol. Catal. A* **159**(2), 327 (2000)
25. A. Varma, A.S. Mukasyan, A.S. Rogachev, K.V. Manukyan, Solution combustion synthesis of nanoscale materials. *Chem. Rev.* **116**, 14493–14586 (2016)
26. P. Erri, P. Pranda, A. Varma, Oxidizer–fuel interactions in aqueous combustion synthesis. 1. iron(III) nitrate–model fuels. *Ind. Eng. Chem. Res.* **43**, 3092–3096 (2004)
27. M.S. Anwar, F. Ahmed, B.H. Koo, Enhanced relative cooling power of Ni_{1-x}Zn_xFe₂O₄ (0.0 ≤ x ≤ 0.7) ferrites. *Acta Mater.* **71**, 100–107 (2014)
28. Y. Köseoğlu, F. Alan, M. Tan, R. Yilgin, M. Öztürk, Low temperature hydrothermal synthesis and characterization of Mn doped cobalt ferrite nanoparticles. *Ceram. Int.* **38**, 3625–3634 (2012)
29. L.N. Anh, T.T. Loan, N.P. Duong, D.T.T. Nguyen, T.D. Hien, Single phase formation, cation distribution, and magnetic characterization of coprecipitated nickel-zinc ferrites. *Anal. Lett.* **48**, 1965–1978 (2015)
30. R.C. Kambale, P.A. Shaikh, S.S. Kamble, Y.D. Kolekar, Effect of cobalt substitution on structural, magnetic and electric properties of nickel ferrite. *J. Alloys Compd.* **478**, 599–603 (2009)
31. M. Hashim, Alimuddin, S. Kumar, S.E. Shirsath, R.K. Kotnala, H. Chung, R. Kumar, Structural properties and magnetic interactions in Ni_{0.5}Mg_{0.5}Fe_{2-x}Cr_xO₄ (0 ≤ x ≤ 1) ferrite nanoparticles. *Powder Technol.* **229**, 37–44 (2012)
32. E. Smidt, K. Meissl, The applicability of Fourier transform infrared (FT-IR) spectroscopy in waste management. *Waste Manag.* **27**, 268 (2007)
33. A.M. Wahba, M.B. Mohamed, Structural, magnetic and dielectric properties of nanocrystalline Cr-substituted Co_{0.8}Ni_{0.2}Fe₂O₄ ferrite. *Ceram. Int.* **40**, 6127 (2014)
34. M.R. Loghman-Estarki, S. Torkian, R.A. Rastabi, A. Ghasemi, Effect of annealing temperature and copper mole ratio on the morphology, structure and magnetic properties of Mg_{0.5-x}Cu_xZn_{0.5}Fe₂O₄ nanoparticles prepared by the modified Pechini method. *J. Magn. Magn. Mater.* **442**, 163–175 (2017)
35. A.R. Rouhani, A.H. Esmaeil-Khanian, F. Davar, S. Hasani, The effect of agarose content on the morphology, phase evolution, and magnetic properties of CoFe₂O₄ nanoparticles prepared by sol-gel autocombustion method. *Int. J. Appl. Ceram. Technol.* **15**, 758–765 (2018)
36. L.D. Zhang, J.M. Mou, *Nanostructured Materials (in Chinese)* (Science Press, Beijing, 2001), pp. 148–152 (**in Chinese**)
37. M. Sertkol, Y. Köseoğlu, A. Baykal, H. Kavasa, A.C. Başaran, Synthesis and magnetic characterization of Zn_{0.6}Ni_{0.4}Fe₂O₄ nanoparticles via a polyethylene glycol-assisted hydrothermal route. *J. Magn. Magn. Mater.* **321**, 157–162 (2009)
38. K.R. Reddy, W. Park, B.C. Sin, J. Noh, Y. Lee, Synthesis of electrically conductive and superparamagnetic monodispersed iron oxide-conjugated polymer composite nanoparticles by in situ chemical oxidative polymerization. *J. Colloid Interface Sci.* **335**, 34–39 (2009)
39. K.R. Reddy, K.P. Lee, J.Y. Kim, Y. Lee, Self-assembly and graft polymerization route to monodispersed Fe₃O₄@SiO₂-polyaniline core-shell composite nanoparticles: physical properties. *J. Nanosci. Nanotechnol.* **8**, 5632–5639 (2008)
40. Y. Köseoğlu, A. Baykal, F. Gözüak, H. Kavas, Structural and magnetic properties of Co_xZn_{1-x}Fe₂O₄ nanocrystals synthesized by microwave method. *Polyhedron* **28**, 2887–2892 (2009)
41. R.H. Kodama, A.E. Berkowitz, E.J. McNiff, S. Foner, Surface spin disorder in NiFe₂O₄ nanoparticles. *Phys. Rev. Lett.* **77**, 394–397 (1996)